batteries

MDPI

Article

A Freestanding Multifunctional Interlayer Based on Fe/Zn Single Atoms Implanted on a Carbon Nanofiber Membrane for High-Performance Li-S Batteries

Mengdi Zhang *, Shuoshuo Kong, Bei Chen and Mingbo Wu *

State Key Laboratory of Heavy Oil Processing, Advanced Chemical Engineering and Energy Materials Research Center, College of New Energy, China University of Petroleum (East China), Qingdao 266580, China; 1903020122@s.upc.edu.cn (S.K.); s22030120@s.upc.edu.cn (B.C.)
* Correspondence: mdzhang@upc.edu.cn (M.Z.); wumb@upc.edu.cn (M.W.)

Abstract: By virtue of the high theoretical energy density and low cost, Lithium–sulfur (Li-S) batteries have drawn widespread attention. However, their electrochemical performances are seriously plagued by the shuttling of intermediate polysulfides and the slow reaction kinetics during practical implementation. Herein, we designed a freestanding flexible membrane composed of nitrogen-doped porous carbon nanofibers anchoring iron and zinc single atoms (FeZn-PCNF), to serve as the polysulfide barrier and the reaction promotor. The flexible porous networks formed by the interwoven carbon nanofibers not only offer fast channels for the transport of electrons/ions, but also guarantee the structural stability of the all-in-one multifunctional interlayer during cycling. Highly dispersed Fe and Zn atoms in the carbon scaffold synergistically immobilize sulfur species and expedite their reversible conversion. Therefore, employing FeZn-PCNF as the freestanding interlayer between the cathode and separator, the Li-S battery delivers a superior initial reversible discharge capacity of 1140 mA h g^{-1} at a current density of 0.5 C and retains a high capacity of 618 mA h g^{-1} after 600 cycles at a high current density of 1 C.

Keywords: freestanding interlayer; carbon nanofibers; metal single atoms; shuttle effect; lithium–sulfur batteries

Citation: Zhang, M.; Kong, S.; Chen, B.; Wu, M. A Freestanding Multifunctional Interlayer Based on Fe/Zn Single Atoms Implanted on a Carbon Nanofiber Membrane for High-Performance Li-S Batteries. *Batteries* **2024**, *10*, 15. https://doi.org/10.3390/batteries10010015

Academic Editor: Seiji Kumagai

Received: 24 November 2023
Revised: 25 December 2023
Accepted: 27 December 2023
Published: 31 December 2023

1. Introduction

Lithium–sulfur (Li-S) batteries are extremely competitive in next-generation secondary batteries, because of high theoretical capacity of both the sulfur cathode (1675 mA h g^{-1}) and the lithium anode (3860 mA h g^{-1}) [1,2]. Also, sulfur has significant superiority in terms of natural abundance, material cost, and environmental benefits [3]. Nevertheless, the commercialization of Li-S batteries has been beset with various difficulties, including the electronic and ionic insulation of S_8 and its solid discharge products (Li_2S_2/Li_2S), the huge volume expansion after discharge, and the shuttle effect of intermediate lithium polysulfides (Li_2S_n, $4 \leq n \leq 8$), which will trigger the active mass loss of both cathode and anode, low Coulombic efficiency, and fast capacity decay [4,5]. There are two main reasons for the shuttle effect: (i) lithium polysulfides can be soluble in an ether-based electrolyte and shuttle between the cathode and the anode [6,7]; (ii) the sluggish redox reaction kinetics between sulfur species will give rise to the accumulation of soluble polysulfides on the cathode side during cycling, thus intensifying the polysulfide shuttling driven by the concentration difference [8,9].

Extensive efforts have been invested in restraining the shuttle effect, such as sulfur host design [10,11], functional separator/ interlayer design [12,13], electrolyte additive utilization [14,15], and sparingly solvating electrolyte utilization [16–18], etc. Among them, the flexible freestanding interlayer can be directly placed between the cathode and separator to act as the physical barrier and the catalyst layer for simultaneously inhibiting

the diffusion of polysulfide and accelerating their conversion reactions. Carbon nanofiber membranes have been used as the freestanding interlayer for Li-S batteries, by virtue of their facile preparation, good mechanical strength, and good flexibility [19–22]. Moreover, the highly conductive carbon network ensures that lithium polysulfides diffused into the interlayer maintain good electronic contact and can be further transformed to solid Li_2S_2/Li_2S during discharge, and then Li_2S_2/Li_2S deposited within the interlayer can be then reversibly converted to soluble polysulfides and return to the cathode side during the charge process. However, relying only on the weak physical confinement effect, lithium polysulfides inevitably escape from the inert carbon nanofiber interlayer during long cycles, and the intrinsic reaction kinetics of sulfur species still remains slow.

The incorporation of metal-based catalysts into the carbon substrate is among the most effective strategies to solve the above problems. These metal-based catalysts, such as metal elements [23,24], metal oxides [25,26], metal sulfides [27,28], metal nitrides [29–31], and heterojunction [32,33], can chemically anchor lithium polysulfides and reduce the redox reaction energy barrier, thus accomplishing the synchronous adsorption–conversion of polysulfides. It is absolutely accepted that the activity of adsorption–catalysis depends highly on the particle size of catalysts because only the surface atoms play these roles. In this regard, single-atom catalysts (SACs) show 100% atomic utilization and afford ample active sites for high-efficiency adsorption and catalysis [6,34,35]. However, the charge and discharge process of Li-S batteries involves multiple intermediates and multistep conversion reactions, where single-component SACs usually play a significant role in a particular aspect only. Zn-SACs show a prominent affinity for polysulfides because the electronegativity of Zn is obviously lower than that of various transition metals, including Fe, Co, and Ni [36]. Such a strong chemical anchoring effect is very favorable for the fast reduction in polysulfides and the uniform deposition of Li_2S [37]. Fe-SACs, as an inexpensive transition metal SAC, have been found to be effective in decreasing the decomposition barrier of insulative Li_2S and thus boosting its oxidation during the charge process [38,39]. Hence, the design of dual-metal Fe/Zn-SACs are expected to combine the advantages of both and enhance the overall electrochemical properties of Li-S batteries.

Here, the nitrogen-doped porous carbon nanofiber membrane implanted with iron and zinc single atoms (FeZn-PCNF) was fabricated by electrospinning combined with a high-temperature pyrolysis approach and directly employed as the freestanding interlayer of Li-S batteries. The porous carbon fibrous framework functions both as the interconnected network for high-efficiency electron/ion convey and as the robust skeleton to intensify the mechanical stability of the interlayer during cycling. The Fe and Zn single-atom active centers can synergistically anchor polysulfides and expedite their bidirectional conversion. Consequently, with the assistance of the multifunctional FeZn-PCNF interlayer, the Li-S batteries afford an impressive initial reversible discharge capacity of 1140 mA h g^{-1} @ 0.5 C and retains a high capacity of 618 mA h g^{-1} after 600 cycles at a high current density of 1C.

2. Experimental

2.1. Synthesis of Binary Zeolitic Imidazolate Frameworks (FeZn-ZIF)

The homogenous solution A and B were prepared by dissolving 1.97 g of 2-methylimidazole in 150 mL of methanol, and dissolving 1.695 g of $Zn(NO_3)_2{\cdot}6H_2O$ and 60 mg of $Fe(NO_3)_3{\cdot}9H_2O$ in 150 mL of methanol, respectively. Then, the solution A and B were rapidly mixed and continued to be stirred for 2 h. The FeZn-ZIF product was obtained after standing for 12 h at 60 °C, followed by centrifugation, washing with methanol several times, and drying in vacuum at 60 °C for 12 h.

2.2. Synthesis of FeZn-PCNF Membrane

An amount of 600 mg of FeZn-ZIF powder, 480 mg of polyacrylonitrile (PAN), and 120 mg of polyvinylpyrrolidone (PVP) were added into 7 mL of *N*,*N*-dimethylformamide (DMF). After stirring vigorously for 24 h, the dispersion was transferred into a syringe for the subsequent electrospinning. During the electrospinning process, the voltage was set to 18 kV,

the feeding rate was set to 0.02 mL min^{-1}, and the distance between the tip of the spinning needle and the collector was 16–18 cm. By heating the as-made fibrous film at 280 °C for 1 h in an air atmosphere and then at 950 °C for 2 h in an N_2 atmosphere, the FeZn-PCNF membrane was obtained. For comparison, the CNF membrane was prepared without the addition of PVP and FeZn-ZIF, and the PCNF membrane was fabricated without the addition of FeZn-ZIF.

2.3. Material Characterizations

The micromorphology was investigated by a scanning electron microscope (SEM, S-4800) and a transmission electron microscope (TEM, JEM-2100F, JEOL Ltd., Tokyo, Japan). The distribution of Fe and Zn single atoms was recognized via high-angle annular dark-field scanning transmission electron microscopy (HAADF-STEM, FEI Tian Cubed Themis G2 300, Shanghai, China). The X-ray diffraction (XRD) was performed on an X'Pert PRO MPD system with Cu *Kα* radiation (λ = 1.5418 Å) with a scan speed of 10 min^{-1}. Pore structure was analyzed on a Micromeritics ASAP 2020 analyzer (Shanghai, China). The X-ray photoelectron spectroscopy (XPS) was detected by Thermo Scientific Escalab 250 XI (Thermo Fisher Scientific, Waltham, MA, USA) with using Al K alpha as the X-ray source of and the charge correction (C 1*s* at 284.8 eV) as the peak calibration procedure. Raman spectra were recorded on Renishaw RM2000 with a 512 nm laser. The mass loading of Fe and Zn atoms was measured via inductively coupled plasma atomic emission spectroscopy (ICP-AES, PerkinElmer, Shanghai, China).

2.4. Adsorption Experiments

S and Li_2S were dissolved in the electrolyte (1.0 M LiTFSI, DOL:DME = 1:1 vol%, 2.0% $LiNO_3$ additive, purchased from DoDo Chem, Suzhou, China) with a molar ratio of 5:1 under intensively stirring at 60 °C to obtain 1 mM of the Li_2S_6 solution. FeZn-PCNF and PCNF, with identical weights, were separately soaked into the Li_2S_6 solution. After resting for 6 h, ultraviolet-visible (UV-vis) spectra of the solution were examined on a UV-vis spectrometer (Shimadzu UV-2700, Kyoto, Japan).

2.5. Symmetrical Cell Measurements

The FeZn-PCNF and PCNF membranes were separately cut into electrode slices with 12 mm of diameter size. The symmetrical cells were then assembled using the identical electrodes as the cathode and anode and 20 μL of the Li_2S_6 solution (0.2 M) as the electrolyte. The cyclic voltammogram (CV) tests were performed on an Ivium-n-Stat electrochemical workstation at 1 mV s^{-1} within −0.8–0.8 V.

2.6. Li-S Cell Measurements

The components of CR2032 coin cells were as follows. The cathode was fabricated by mixing the carbon nanotubes/sulfur mixture (CNTs/S), super P, and polyvinylidene fluoride with a mass ratio of 7:2:1 in the N-Methylpyrrolidone solvent. The mixed slurry was cast onto the Al foil and cut into disks with 12 mm diameter after drying. The sulfur mass loading in the CNTs/S cathode was around 1.2 mg cm^{-2}. The anode was lithium foil, the separator was polypropylene (PP) membrane, the electrolyte was 1.0 M LiTFSI dispersed in the DME/DOL solution (1:1 vol%) with 2.0 wt.% of the $LiNO_3$ additive, and the interlayer is FeZn-PCNF or PCNF membranes. The electrolyte/sulfur (E/S) ratio was 19 μL mg^{-1}. The CV curves in the voltage range of 1.7–2.8 V and the electrochemical impedance spectroscopy (EIS) in the frequency range of 0.00001–100 kHz of the as-assembled Li-S batteries were measured on the Iviumn-Stat electrochemical workstation. The galvanostatic charge and discharge (GCD) tests were conducted on a Land CT2001A system in the voltage range of 1.7–2.8 V.

3. Results and Discussion

The fabrication procedure of the FeZn-PCNF membrane is illustrated as Figure 1. Briefly, the FeZn-ZIF precursor was first synthesized via the coordination of binary metal

ions (Fe^{2+} and Zn^{2+}) and 2-methylimidazole ligands. The SEM images (Figure S1) indicate that FeZn-ZIF presented a typical polyhedral morphology with a uniform size. The fibrous membrane composited of PAN, PVP, and FeZn-ZIF was then fabricated by using electrospinning technology. As shown in the SEM image (Figure S2a), a multitude of nanofibers are interwoven together to form a network structure. The SEM image at higher magnification (Figure S2b) further shows a rough and uneven surface of nanofibers, indicating the successful incorporation of FeZn-ZIF polyhedrons. During the subsequent high-temperature pyrolysis process, the FeZn-ZIF polyhedrons provided a stable confined space to inhibit the agglomeration of metallic atoms, and the evaporation of partial Zn out of the FeZn-ZIF skeleton not only created many micropores in the nanofibers, but more importantly, it left behind more nitrogen sites to immobilize residual Zn and Fe atoms via the M-N_x coordination structure [36,37,40,41]. In addition, PVP molecules were degraded and thus further enriched the pore structure of carbon nanofibers. The intact fibrous membrane structure was well inherited after pyrolysis. The thickness and mass of the FeZn-PCNF interlayer are 60 μm and 1 mg, respectively. Figure S3 shows it can be folded at various angles and ultimately returned to the original state, demonstrating its good structural flexibility and mechanical stability, which are beneficial to keep the integrity during long cycling when used as the multifunctional interlayer.

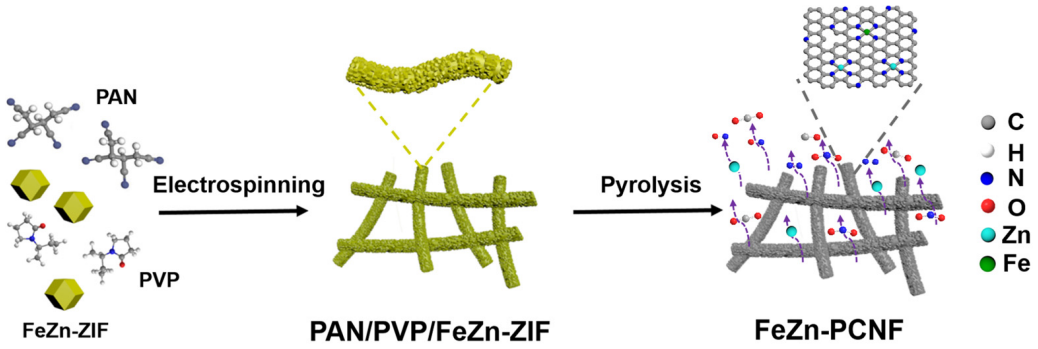

Figure 1. Synthesis process illustration of FeZn-PCNF membrane.

The micromorphology and structure of FeZn-PCNF membrane can be observed from Figure 2. The SEM image (Figure 2a) depicts a network structure interwoven by many elongated nanofibers with rough surface, endowing FeZn-PCNF with a good flexibility and mechanical stability. Also, a large quantity of holes between the staggered nanofibers are beneficial to the immersion and transport of the electrolyte. The TEM image (Figure 2b,c) further shows the existence of many hollow polyhedral boxes, which are derived from the pyrolysis of the FeZn-ZIF precursors within nanofibers, which can function as the reservoirs for soluble polysulfides. In addition, no metal aggregation was observed in FeZn-PCNF, indicating the high dispersion of metallic atoms. The HAADF-STEM image at an atomic size (Figure 2d) further reveals that a wealth of isolated Fe/Zn atoms (seen as bright spots) are randomly distributed throughout the nanofibrous membrane, which is also confirmed by the STEM image and the corresponding EDS elemental mapping (Figure 2e–i).

A similar phase structure is demonstrated by the XRD patterns of FeZn-PCNF and PCNF. As shown in Figure 3a, there is only a broad peak at 25.4°, which is corresponding to the (002) crystal plane of non-graphitized carbon. No peaks associated with iron and zinc occur, further suggesting the amorphous state of metallic atoms. The Raman spectra (Figure 3b) of both FeZn-PCNF and PCNF exhibit two main peaks at 1354 cm^{-1} and 1587 cm^{-1}, corresponding to the typical D band (disorder and defects in carbon) and G band (graphitic SP^2 carbon), respectively. Moreover, the defect degree can be revealed by the peak intensity ratio of D and G bands (I_D/I_G). The I_D/I_G value for FeZn-PCNF is 1.08, far higher than that for PCNF (0.97), which can be ascribed to a more defective structure derived from the doping of N, Fe, and Zn atoms. As can be seen from the N_2 adsorption and desorption isotherms (Figure 3c), PCNF shows type-I isotherms, which

are characteristic of a micropore structure [42], but FeZn-PCNF shows type-VI isotherms, indicating both micropores and mesopores in FeZn-PCNF [43]. In contrast, CNF exhibits negligible adsorption for N_2, revealing a nonporous structure (Figure S4). The specific surface area of FeZn-PCNF, PCNF, and CNF are 237, 169, and 30 m^2 g^{-1}, respectively, fully demonstrating the pore-forming effects derived from the PVP pyrolysis and the incomplete evaporation of Zn from the ZIF-derived carbon skeleton. The pore size distribution curves in the inset of Figure 3c also reveal a more developed porous structure of FeZn-PCNF, which will be beneficial to exposing more active sites and accelerating ion diffusion. The surface chemical compositions of FeZn-PCNF and PCNF were identified by XPS spectra. As seen from Figure 3d, the full XPS survey spectra show that both FeZn-PCNF and PCNF contain C, O, and N elements. In addition, Zn $2p_{1/2}$ and Zn $2p_{3/2}$ peaks were detected in FeZn-PCNF, indicating that there is still residual Zn after pyrolysis. No elemental Fe signal was observed resulting from the limited detection depth of XPS [39]. The mass loading of Fe and Zn single atoms in FeZn-PCNF was tested as 0.78 wt.% and 1.25 wt.% via ICP-AES. The C 1*s* spectra of FeZn-PCNF and PCNF (Figure S5a,b) can be deconvoluted into three sub-peaks assigned to C–C/C=C, C-N, and C=O bonds [44,45]. With regard to the N 1*s* spectra (Figure 3e,f), the N element exists in four forms, including pyridinic N (398.0 eV), pyrrolic N (399.6 eV), graphitic N (400.7 eV), and oxidized N (402.9 eV) [46]. The proportion of various N species is displayed in Table S1. It is found that pyridinic N is significantly increased and dominates in FeZn-PCNF, which may originate from the nitrogen species in the FeZn-ZIF precursor. The abundant pyridinic N provides stable coordination sites for the monatomic dispersion of Fe and Zn, and its inherent electron-rich characteristic results in a good affinity for polar polysulfides [47–49]. All of the characterization results demonstrate that dual-metal Fe and Zn single atoms are evenly implanted in the porous and flexible carbon nanofiber network, which are expected to enhance the chemical adsorption for polysulfides and expedite the redox reaction during cycles.

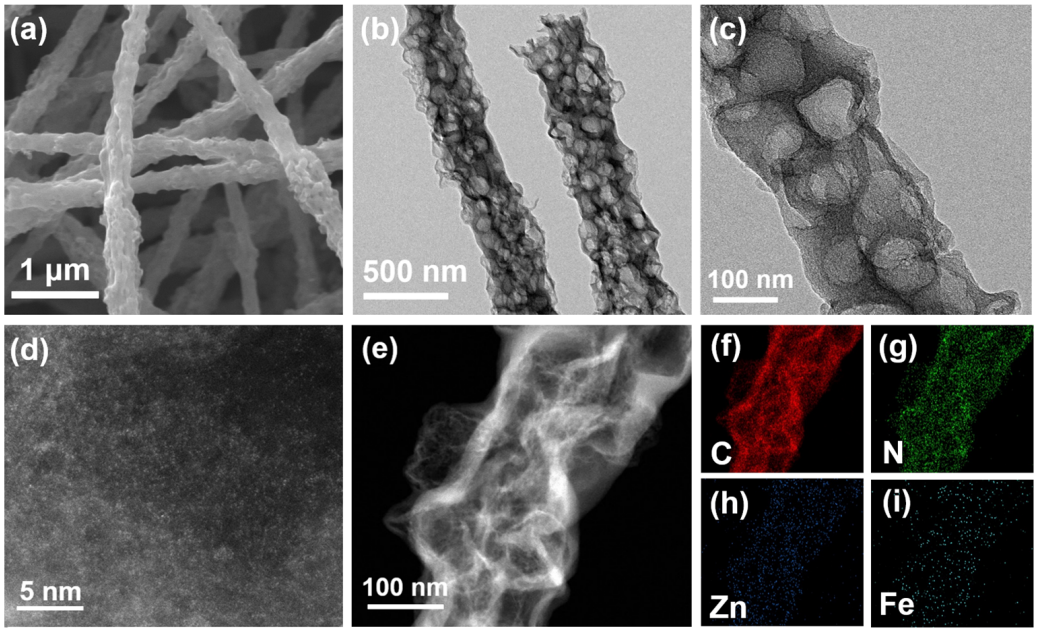

Figure 2. Micromorphology and structure of FeZn-PCNF. (**a**) SEM image, (**b**,**c**) TEM images, (**d**) HAADF-STEM image, and (**e**) STEM image and the corresponding EDS elemental mapping of (**f**) C, (**g**) N, (**h**) Zn, and (**i**) Fe.

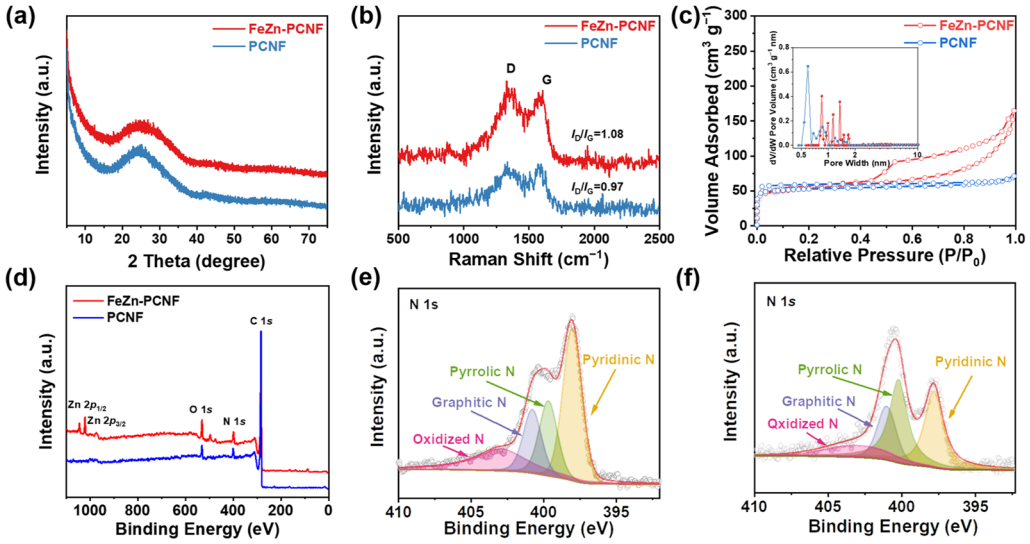

Figure 3. (**a**) XRD patterns, (**b**) Raman spectra, (**c**) N_2 adsorption–desorption isotherms with the inset of the corresponding pore size distribution curves, (**d**) full XPS spectra of FeZn-PCNF and PCNF; and high-resolution XPS spectra of N 1s in (**e**) FeZn-PCNF and (**f**) PCNF.

The adsorption capability of FeZn-PCNF and PCNF membranes for soluble polysulfides was evaluated by visualized adsorption tests. As displayed in Figure 4a, the Li_2S_6 solution still shows as brownish yellow after adding PCNF, whereas the Li_2S_6 solution containing FeZn-PCNF become almost colorless. The clear supernatant of the Li_2S_6 solution after adsorption was characterized by the UV-vis spectra. Compared with the Li_2S_6 solution after being adsorbed via PCNF, the absorption peak of S_6^{2-} was hardly detected in the Li_2S_6 solution after being adsorbed via FeZn-PCNF. These comparative results manifest that the FeZn-PCNF interlayer has a potent adsorption for polysulfides, which is attributed to the comprehensive advantages including the physical adsorption by well-developed pores and the chemical anchoring by M-N_x active centers. The electrocatalytic activity of FeZn-PCNF and PCNF was further evaluated by the CV measurements of symmetrical batteries containing the Li_2S_6 electrolyte. As reveled by Figure 4b, FeZn-PCNF exhibits stronger current responses with three pairs of notable redox peaks, demonstrating higher catalytic activity for the bidirectional conversion of polysulfide. By virtue of the superior adsorption–catalysis effect, the FeZn-PCNF interlayer endows the Li-S batteries with improved electrochemical performances. The CV curves of FeZn-PCNF- and PCNF-based Li-S batteries at 0.1 mV s^{-1} are exhibited in Figure 4c. The cathodic peaks C1 and C2 are attributable to the reduction of S_8 to soluble lithium polysulfides and lithium polysulfides to insoluble Li_2S/Li_2S_2, respectively. The anodic peaks A1 and A2 are assigned to the processes of Li_2S_2/Li_2S back to soluble lithium polysulfides and finally to S_8 [50,51]. in addition, the Li-S battery with the FeZn-PCNF interlayer exhibits much faster current response and smaller polarization, indicating that a more powerful catalytic effect on the reversible transformation of sulfur species. Furthermore, the CV curves of the Li-S batteries with the FeZn-PCNF and PCNF interlayers were measured at different scan rates (Figure S6), and the diffusion coefficient of lithium ion (D_{Li}) was calculated based on the Randles–Sevcik equation [21,52]:

$$I_p = \left(2.69 \times 10^5\right) n^{1.5} A D_{Li}^{0.5} v^{0.5} C_{Li}$$

where I_p refers to the peak current (A), n refers to the number of charge transfers in the reaction (n = 2), A refers to the electrode area (1.13 cm^2), v refers to the scan rate (mV s^{-1}), and C_{Li} refers to the lithium ion concentration in the electrolyte. Herein, the I_p values increase with the increase in the scan rate and follow a linear relationship with $v^{0.5}$ as revealed by Figure 4d,e. Obviously, a larger slope suggests a faster Li-ion diffusion. As seen from Figure 4f, the D_{Li}

values of the FeZn-PCNF-based Li-S battery are 2.67×10^{-7}, 3.00×10^{-7}, 5.11×10^{-8}, and 1.60×10^{-7} cm^3 s^{-1} for the peaks A1, A2, C1, and C2, respectively, all of which are higher than those of the PCNF-based Li-S battery, demonstrating accelerated diffusion kinetics of lithium ions in the FeZn-PCNF interlayer. The EIS spectra (Figure S7) show that the charge transfer resistance of the FeZn-PCNF-based Li-S battery is much smaller than that of the PCNF-based Li-S battery, which indicates that FeZn-PCNF has higher electronic conductivity and faster interfacial catalytic activity [53].

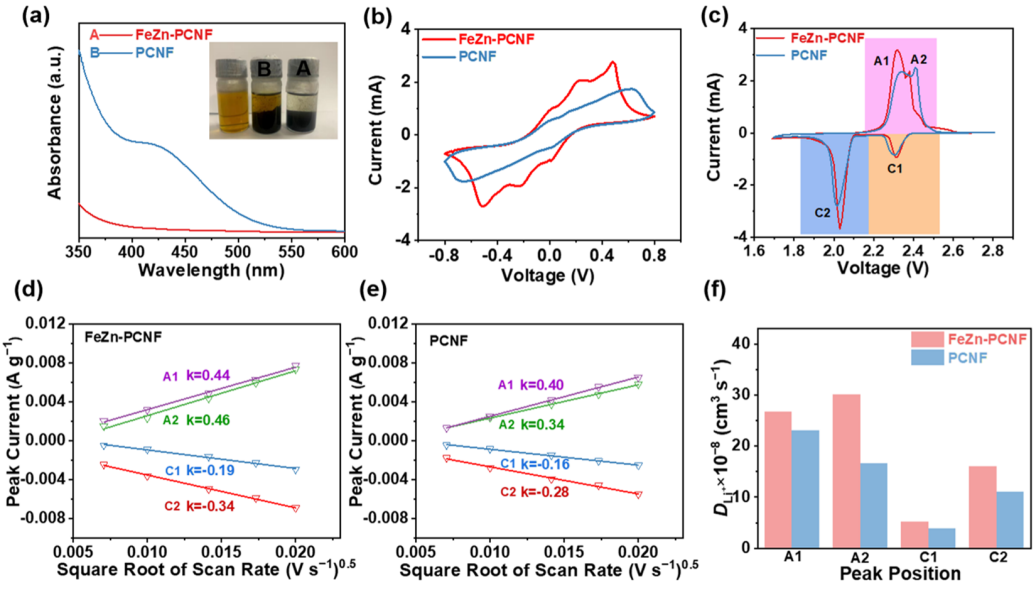

Figure 4. (**a**) UV-vis spectra and digital images of Li_2S_6 solution before and after adding FeZn-PCNF and PCNF absorbents, (**b**) CV curves of Li_2S_6 symmetric cells using FeZn-PCNF and PCNF electrodes, (**c**) CV curves of the FeZn-PCNF- and PCNF- based Li-S batteries at 0.1 mV s^{-1}. Linear fitting of redox peak currents of the (**d**) FeZn-PCNF- and (**e**) PCNF- based Li-S batteries for Peaks A1, A2, C1 and C2, and (**f**) D_{Li} values of the FeZn-PCNF- and PCNF- based Li-S batteries for peaks A1, A2, C1 and C2.

The cycling performances of the FeZn-PCNF- and PCNF- based Li-S batteries were evaluated at 0.5 C. As displayed in Figure 5a, the initial specific capacity of the PCNF-based Li-S battery is 1021 mA h g^{-1} and maintains at only 660 mA h g^{-1} after 200 cycles, but the FeZn-PCNF-based Li-S battery delivers an initial specific capacity up to 1140 mA h g^{-1} and a high retained capacity of 795 mA h·g^{-1} after 200 cycles, suggesting a higher active mass utilization and a superior cycling stability. Furthermore, the microstructure and composition of the FeZn-PCNF interlayer after cycles were investigated. As observed from Figure S8a, sulfur is uniformly deposited on the surface of the nanofibrous film without large agglomerations. The EDS mappings (Figure S8b–g) show the even dispersion of C, N, Fe, Zn, and S elements. The above results confirm that the active materials would be immobilized in this conductive interlayer and be utilized during cycling. The GCD curves of both Li-S batteries (Figure S9) show two discharge plateaus and a long charge plateau. The high and low discharge plateaus correspond to the conversion from solid S_8 to soluble Li_2S_n and the conversion from Li_2S_4 to solid Li_2S_2/Li_2S, respectively, and the charge plateau corresponds to the inverse conversion process [54]. It differs in that the FeZn-PCNF-based battery exhibits a lower potential gap (ΔE), implying that M-N_x active centers can propel the reaction kinetics of sulfur species. The capacity contribution at high and low discharge plateaus was further analyzed in Figure 5b,c. The generation of a high-plateau capacity (Q_H) is accompanied by the intractable shuttling of polysulfides, and the low-plateau capacity (Q_L) is restricted by the incomplete conversion due to the sluggish and nonuniform Li_2S_2/Li_2S deposition [55,56]. As revealed by Figure 5d,e, the values of Q_H and Q_L of the FeZn-PCNF-based Li-S battery are always higher than those

of the PCNF-based Li-S battery along with the cycles, which fully demonstrates that the FeZn-PCNF interlayer can effectively intercept the polysulfide crossover and induce the fast and uniform deposition of solid Li_2S_2/Li_2S. The rate performances of the batteries based on two interlayers are shown in Figure 5f. The capacities of the FeZn-PCNF-based Li-S battery are 1421, 1103, 1013, and 926 mA h g^{-1} at 0.2, 0.5, 1, and 2 C, respectively, all of which are much higher than those of the PCNF-based Li-S battery. Besides, the FeZn-PCNF-based Li-S battery still delivers a decent specific capacities based on the total mass of the cathode and the interlayer (Figure S10). Figure 5g shows the long cycling performance of the FeZn-PCNF-based battery at 1 C. After five cycles of activation, the discharge capacity is up to 949 mA h g^{-1} and a high capacity of 618 mA h g^{-1} is retained after 600 cycles, corresponding to a low capacity decay of only 0.06% per cycle. Based on the above discussion, the FeZn-PCNF interlayer is responsible for admirable rate and cycling performances of the Li-S batteries. The synergistic work mechanism of Fe and Zn active centers is illustrated in Figure 5h. During the discharge process, atomic Zn sites with a low electronegativity strongly capture soluble polysulfides and accelerate their reduction reaction, thus regulating the uniform deposition of insulative Li_2S. During the ensuing charge process, the Fe-N_x active sites decrease the energy barrier of the Li_2S decomposition, thus kinetically favoring the oxidation reaction from Li_2S to S. Therefore, the polysulfide shuttling is effectively mitigated and the reversible solid–liquid–solid conversion reactions are significantly boosted.

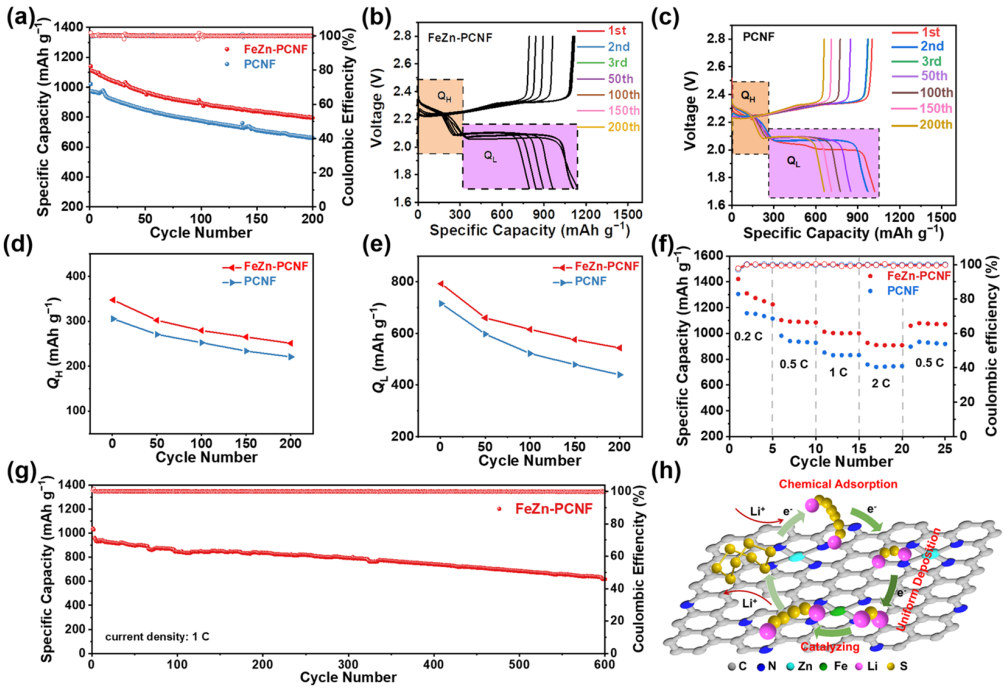

Figure 5. (**a**) Cycling performances of the FeZn-PCNF- and PCNF- based Li-S batteries at 0.5 C, GCD curves of the (**b**) FeZn-PCNF- and (**c**) PCNF- based Li-S batteries at different cycles, variation in (**d**) Q_H and (**e**) Q_L of the FeZn-PCNF- and PCNF- based Li-S batteries during cycles, (**f**) rate performances of the FeZn-PCNF- and PCNF- based Li-S batteries, (**g**) long cycling performance of the FeZn-PCNF-based Li-S battery at 1 C, and (**h**) schematic illustration of the work mechanism of FeZn-PCNF interlayer.

4. Conclusions

In summary, a freestanding FeZn-PCNF interlayer was successfully developed by electrospinning followed by the high-temperature pyrolysis method to physically block polysulfides and regulate sulfur chemistry. The flexible and conductive carbon skeleton serves as the interconnected "expressway network" to speed up the migration of electrons and lithium ions. With assistance from the spatial confinement of FeZn-ZIF polyhedrons and

the strong anchoring of ample nitrogen atoms, Fe and Zn single atoms are uniformly doped into the carbon fibrous network and synergistically contribute to enhancing the chemical immobilization for polysulfides and propelling the redox reaction kinetics. Benefiting from these comprehensive advantages, the FeZn-PCNF-based Li-S battery demonstrates a high specific capacity of 1224 mA h g^{-1} at 0.2 C and a high capacity retention of 908 mA h g^{-1} even at 2 C. Meanwhile, the battery achieves an excellent cycling performance with a capacity decay of only 0.06% per cycle over 600 cycles at 1 C. This work offers a feasible and appealing route to the design of dual-metal SACs towards high-efficiency Li-S batteries and other electrochemical systems involving multi-order reactions.

Supplementary Materials: The following supporting information can be downloaded at: https://www.mdpi.com/article/10.3390/batteries10010015/s1. Figure S1: SEM images of FeZn-ZIF; Figure S2: SEM images of PAN/PVP/FeZn-ZIF nanofiber membrane; Figure S3: Optical photographs of FeZn-PCNF membrane at different fold angles; Figure S4: N_2 adsorption–desorption isotherms of CNF; Figure S5: High-resolution C *1s* XPS spectra; Figure S6: CV curves; Figure S7: EIS spectra; Figure S8: SEM-EDS images of FeZn-PCNF interlayer after cycles; Figure S9: GCD curves; Figure S10: Discharge capacities of the Li-S batteries based on the total mass of cathode and interlayer; Table S1: Proportion of various N species in FeZn-PCNF and PCNF.

Author Contributions: M.Z.: conceptualization, methodology, investigation, and writing—review and editing; S.K. and B.C.: investigation and data curation; M.W.: supervision and resources. All authors have read and agreed to the published version of the manuscript.

Funding: This work was supported by the National Natural Science Foundation of China (22005341 and 22138013), the Shandong Provincial Natural Science Foundation (ZR2020QB128 and ZR2020ZD08), the Taishan Scholar Project (tsqnz20221121 and ts201712020), and the Major Scientific and Technological Innovation Project of Shandong Province (2020CXGC010402).

Data Availability Statement: The data presented in this study are available on request from the corresponding author. The data are not publicly available due to privacy.

Conflicts of Interest: The authors declare no conflicts of interest.

References

1. Shao, Q.; Zhu, S.; Chen, J. A Review on Lithium-Sulfur Batteries: Challenge, Development, and Perspective. *Nano Res.* **2023**, *16*, 8097–8138. [CrossRef]
2. Yin, Y.-X.; Xin, S.; Guo, Y.-G.; Wan, L.-J. Lithium-Sulfur Batteries: Electrochemistry, Materials, and Prospects. *Angew. Chem. Int. Ed.* **2013**, *52*, 13186–13200. [CrossRef] [PubMed]
3. Zhang, M.; Chen, B.; Wu, M. Research Progress in Graphene as Sulfur Hosts in Lithium-Sulfur Batteries. *Acta Phys. Chim. Sin.* **2022**, *38*, 2101001. [CrossRef]
4. Mccreary, C.; An, Y.; Kim, S.U.; Hwa, Y. A Perspective on Li/S Battery Design: Modeling and Development Approaches. *Batteries* **2021**, *7*, 82. [CrossRef]
5. He, J.; Manthiram, A. A Review on the Status and Challenges of Electrocatalysts in Lithium-Sulfur Batteries. *Energy Storage Mater.* **2019**, *20*, 55–70. [CrossRef]
6. Zhuang, Z.; Kang, Q.; Wang, D.; Li, Y. Single-Atom Catalysis Enables Long-Life, High-Energy Lithium-Sulfur Batteries. *Nano Res.* **2020**, *13*, 1856–1866. [CrossRef]
7. Manthiram, A.; Fu, Y.; Chung, S.-H.; Zu, C.; Su, Y.-S. Rechargeable Lithium-Sulfur Batteries. *Chem. Rev.* **2014**, *114*, 11751–11787. [CrossRef]
8. Wang, P.; Xi, B.; Huang, M.; Chen, W.; Feng, J.; Xiong, S. Emerging Catalysts to Promote Kinetics of Lithium-Sulfur Batteries. *Adv. Energy Mater.* **2021**, *11*, 2002893. [CrossRef]
9. Lim, W.-G.; Kim, S.; Jo, C.; Lee, J. A Comprehensive Review of Materials with Catalytic Effects in Li-S Batteries: Enhanced Redox Kinetics. *Angew. Chem. Int. Ed.* **2019**, *58*, 18746–18757. [CrossRef]
10. Li, F.; Liu, Q.H.; Hu, J.W.; Feng, Y.Z.; He, P.B.; Ma, J.M. Recent Advances in Cathode Materials for Rechargeable Lithium-Sulfur Batteries. *Nanoscale* **2019**, *11*, 15418–15439. [CrossRef]
11. Zhang, M.; Yu, C.; Yang, J.; Zhao, C.; Ling, Z.; Qiu, J. Nitrogen-Doped Tubular/Porous Carbon Channels Implanted on Graphene Frameworks for Multiple Confinement of Sulfur and Polysulfides. *J. Mater. Chem. A* **2017**, *5*, 10380–10386. [CrossRef]
12. Hao, H.; Hutter, T.; Boyce, B.L.; Watt, J.; Liu, P.; Mitlin, D. Review of Multifunctional Separators: Stabilizing the Cathode and the Anode for Alkali (Li, Na, and K) Metal-Sulfur and Selenium Batteries. *Chem. Rev.* **2022**, *122*, 8053–8125. [CrossRef] [PubMed]
13. Fan, L.; Li, M.; Li, X.; Xiao, W.; Chen, Z.; Lu, J. Interlayer Material Selection for Lithium-Sulfur Batteries. *Joule* **2019**, *3*, 361–386. [CrossRef]

14. Li, W.; Yao, H.; Yan, K.; Zheng, G.; Liang, Z.; Chiang, Y.-M.; Cui, Y. The Synergetic Effect of Lithium Polysulfide and Lithium Nitrate to Prevent Lithium Dendrite Growth. *Nat. Commun.* **2015**, *6*, 7436. [CrossRef] [PubMed]
15. Liu, C.; Wu, H.; Wu, J.; Xiao, Y.; Deng, Y. Dual-Functional Electrolyte Additive for Lithium-Sulfur Batteries Limits Lithium Dendrite Formation and Increases Sulfur Utilization Rate. *Batteries* **2023**, *9*, 444. [CrossRef]
16. Long, H.-L.; Peng, H.-J. Encapsulating-Polysulfide Electrolyte: An Answer to Practical Lithium-Sulfur Batteries. *Chin. Chem. Lett.* **2023**, *34*, 108033. [CrossRef]
17. Ye, H.; Li, Y. Towards Practical Lean-Electrolyte Li–S Batteries: Highly Solvating Electrolytes or Sparingly Solvating Electrolytes? Nano Res. *Energy* **2022**, *1*, 9120012. [CrossRef]
18. Castillo, J.; Soria-Fernández, A.; Rodriguez-Peña, S.; Rikarte, J.; Robles-Fernández, A.; Aldalur, I.; Cid, R.; González-Marcos, J.A.; Carrasco, J.; Armand, M.; et al. Graphene-Based Sulfur Cathodes and Dual Salt-Based Sparingly Solvating Electrolytes: A Perfect Marriage for High Performing, Safe, and Long Cycle Life Lithium-Sulfur Prototype Batteries. *Adv. Energy Mater.* **2023**, 2302378. [CrossRef]
19. Huang, J.Q.; Zhang, B.A.; Xu, Z.L.; Abouali, S.; Garakani, M.A.; Huang, J.Q.; Kim, J.K. Novel Interlayer Made from Fe_3C/Carbon Nanofiber Webs for High Performance Lithium-Sulfur Batteries. *J. Power Sources* **2015**, *285*, 43–50. [CrossRef]
20. Tu, S.; Chen, X.; Zhao, X.; Cheng, M.; Xiong, P.; He, Y.; Zhang, Q.; Xu, Y. A Polysulfide-Immobilizing Polymer Retards the Shuttling of Polysulfide Intermediates in Lithium–Sulfur Batteries. *Adv. Mater.* **2018**, *30*, 1804581. [CrossRef]
21. Hu, F.; Peng, H.; Zhang, T.; Shao, W.; Liu, S.; Wang, J.; Wang, C.; Jian, X. A Lightweight Nitrogen/Oxygen Dual-Doping Carbon Nanofiber Interlayer with Meso-/Micropores for High-Performance Lithium-Sulfur Batteries. *J. Energy Chem.* **2021**, *58*, 115–123. [CrossRef]
22. Saroha, R.; Oh, J.H.; Seon, Y.H.; Kang, Y.C.; Lee, J.S.; Jeong, D.W.; Cho, J.S. Freestanding Interlayers for Li-S Batteries: Design and Synthesis of Hierarchically Porous N-Doped C Nanofibers Comprising Vanadium Nitride Quantum Dots and MOF-Derived Hollow N-Doped C Nanocages. *J. Mater. Chem. A* **2021**, *9*, 11651–11664. [CrossRef]
23. Zhang, M.; Yu, C.; Zhao, C.; Song, X.; Han, X.; Liu, S.; Hao, C.; Qiu, J. Cobalt-Embedded Nitrogen-Doped Hollow Carbon Nanorods for Synergistically Immobilizing the Discharge Products in Lithium–Sulfur Battery. *Energy Storage Mater.* **2016**, *5*, 223–229. [CrossRef]
24. Tsao, Y.; Gong, H.; Chen, S.; Chen, G.; Liu, Y.; Gao, T.Z.; Cui, Y.; Bao, Z. A Nickel-Decorated Carbon Flower/Sulfur Cathode for Lean-Electrolyte Lithium–Sulfur Batteries. *Adv. Energy Mater.* **2021**, *11*, 2101449. [CrossRef]
25. Salhabi, E.H.M.; Zhao, J.; Wang, J.; Yang, M.; Wang, B.; Wang, D. Hollow Multi-Shelled Structural TiO_{2-X} with Multiple Spatial Confinement for Long-Life Lithium-Sulfur Batteries. *Angew. Chem. Int. Ed.* **2019**, *58*, 9078–9082. [CrossRef] [PubMed]
26. Li, R.; Rao, D.; Zhou, J.; Wu, G.; Wang, G.; Zhu, Z.; Han, X.; Sun, R.; Li, H.; Wang, C.; et al. Amorphization-Induced Surface Electronic States Modulation of Cobaltous Oxide Nanosheets for Lithium-Sulfur Batteries. *Nat. Commun.* **2021**, *12*, 3102. [CrossRef]
27. Zhang, J.; Yu, L.; Lou, X.W. Embedding CoS_2 Nanoparticles in N-Doped Carbon Nanotube Hollow Frameworks for Enhanced Lithium Storage Properties. *Nano Res.* **2017**, *10*, 4298–4304. [CrossRef]
28. He, J.; Chen, Y.; Manthiram, A. Metal Sulfide-Decorated Carbon Sponge as a Highly Efficient Electrocatalyst and Absorbant for Polysulfide in High-Loading Li_2S Batteries. *Adv. Energy Mater.* **2019**, *9*, 1900584. [CrossRef]
29. Lim, W.-G.; Jo, C.; Cho, A.; Hwang, J.; Kim, S.; Han, J.W.; Lee, J. Approaching Ultrastable High-Rate Li-S Batteries through Hierarchically Porous Titanium Nitride Synthesized by Multiscale Phase Separation. *Adv. Mater.* **2019**, *31*, 1806547. [CrossRef]
30. Li, R.; Peng, H.; Wu, Q.; Zhou, X.; He, J.; Shen, H.; Yang, M.; Li, C. Sandwich-Like Catalyst-Carbon-Catalyst Trilayer Structure as a Compact 2D Host for Highly Stable Lithium-Sulfur Batteries. *Angew. Chem. Int. Ed.* **2020**, *59*, 12129–12138. [CrossRef]
31. Yue, X.-Y.; Zhang, J.; Bao, J.; Bai, Y.-F.; Li, X.-L.; Yang, S.-Y.; Fu, Z.-W.; Wang, Z.-H.; Zhou, Y.-N. Sputtered MoN Nanolayer as a Multifunctional Polysulfide Catalyst for High-Performance Lithium–Sulfur Batteries. *eScience* **2022**, *2*, 329–338. [CrossRef]
32. Shi, K.; Sun, Y.; Xiong, Z.; Li, J.; Nan, H.; Lin, Y.; Wei, Z.; Liu, Q. Achieving Balanced Behavior between Polysulfides Adsorption and Catalytic Conversion from Heterostructure Fe_3C-Fe_3P Promotor for High-Performance Lithium-Sulfur Batteries. *Chem. Eng. J.* **2023**, *460*, 141794. [CrossRef]
33. Zhang, M.; Mu, J.; Li, Y.; Pan, Y.; Dong, Z.; Chen, B.; Guo, S.; Yuan, W.; Fang, H.; Hu, H.; et al. Propelling Polysulfide Redox by Fe_3C-FeN Heterostructure@Nitrogen-Doped Carbon Framework Towards High-Efficiency Li-S Batteries. *J. Energy Chem.* **2023**, *78*, 105–114. [CrossRef]
34. Fang, L.Z.; Feng, Z.E.; Cheng, L.; Winans, R.E.; Li, T. Design Principles of Single Atoms on Carbons for Lithium-Sulfur Batteries. *Small Methods* **2020**, *4*, 2000315. [CrossRef]
35. Xiao, R.; Chen, K.; Zhang, X.; Yang, Z.; Hu, G.; Sun, Z.; Cheng, H.-M.; Li, F. Single-Atom Catalysts for Metal-Sulfur Batteries: Current Progress and Future Perspectives. *J. Energy Chem.* **2021**, *54*, 452–466. [CrossRef]
36. Song, K.; Feng, Y.; Zhou, X.; Qin, T.; Zou, X.; Qi, Y.; Chen, Z.; Rao, J.; Wang, Z.; Yue, N.; et al. Exploiting the Trade-Offs of Electron Transfer in Mof-Derived Single Zn/Co Atomic Couples for Performance-Enhanced Zinc-Air Battery. *Appl. Catal. B-Environ.* **2022**, *316*, 121591. [CrossRef]
37. Wu, J.; Feng, Y.; Chen, Y.; Fan, T.; Li, Y. Double-Shelled Zn–Co Single-Atoms Enable Enhanced Conversion Kinetics in Lithium–Sulfur Batteries. *J. Mater. Chem. A* **2023**, *11*, 12025–12033. [CrossRef]

38. Zhou, G.; Zhao, S.; Wang, T.; Yang, S.-Z.; Johannessen, B.; Chen, H.; Liu, C.; Ye, Y.; Wu, Y.; Peng, Y.; et al. Theoretical Calculation Guided Design of Single-Atom Catalysts toward Fast Kinetic and Long-Life Li-S Batteries. *Nano Lett.* **2020**, *20*, 1252–1261. [CrossRef]
39. Wang, C.; Song, H.; Yu, C.; Ullah, Z.; Guan, Z.; Chu, R.; Zhang, Y.; Zhao, L.; Li, Q.; Liu, L. Iron Single-Atom Catalyst Anchored on Nitrogen-Rich Mof-Derived Carbon Nanocage to Accelerate Polysulfide Redox Conversion for Lithium Sulfur Batteries. *J. Mater. Chem. A* **2020**, *8*, 3421–3430. [CrossRef]
40. Yang, J.-L.; Yang, P.; Cai, D.-Q.; Wang, Z.; Fan, H.J. Atomically Dispersed Fe–N_4 and Ni–N_4 Independent Sites Enable Bidirectional Sulfur Redox Electrocatalysis. *Nano Lett.* **2023**, *23*, 4000–4007. [CrossRef]
41. Zhang, H.; Hwang, S.; Wang, M.; Feng, Z.; Karakalos, S.; Luo, L.; Qiao, Z.; Xie, X.; Wang, C.; Su, D.; et al. Single Atomic Iron Catalysts for Oxygen Reduction in Acidic Media: Particle Size Control and Thermal Activation. *J. Am. Chem. Soc.* **2017**, *139*, 14143–14149. [CrossRef] [PubMed]
42. Zhang, M.; Yu, C.; Ling, Z.; Yu, J.; Li, S.; Zhao, C.; Huang, H.; Qiu, J. A Recyclable Route to Produce Biochar with a Tailored Structure and Surface Chemistry for Enhanced Charge Storage. *Green Chem.* **2019**, *21*, 2095–2103. [CrossRef]
43. Zhang, P.; Sun, F.; Xiang, Z.; Shen, Z.; Yun, J.; Cao, D. Zif-Derived in Situ Nitrogen-Doped Porous Carbons as Efficient Metal-Free Electrocatalysts for Oxygen Reduction Reaction. *Energy Environ. Sci.* **2014**, *7*, 442–450. [CrossRef]
44. Zou, J.; Dong, H.; Wu, H.; Huang, J.; Zeng, X.; Dou, Y.; Yao, Y.; Li, Z. Laser-Induced Rapid Construction of Co/N-Doped Honeycomb-Like Carbon Networks as Oxygen Electrocatalyst Used in Zinc-Air Batteries. *Carbon* **2022**, *200*, 462–471. [CrossRef]
45. Wang, F.; Liao, X.; Wang, H.; Zhao, Y.; Mao, J.; Truhlar, D.G. Bioinspired Mechanically Interlocking Holey Graphene@SiO_2 Anode. *Interdiscip. Mater.* **2022**, *1*, 517–525. [CrossRef]
46. Sun, W.; Liu, S.; Li, Y.; Wang, D.; Guo, Q.; Hong, X.; Xie, K.; Ma, Z.; Zheng, C.; Xiong, S. Monodispersed FeS_2 Electrocatalyst Anchored to Nitrogen-Doped Carbon Host for Lithium–Sulfur Batteries. *Adv. Funct. Mater.* **2022**, *32*, 2205471. [CrossRef]
47. Han, J.; Meng, X.; Lu, L.; Bian, J.; Li, Z.; Sun, C. Single-Atom Fe-N_x-C as an Efficient Electrocatalyst for Zinc–Air Batteries. *Adv. Funct. Mater.* **2019**, *29*, 1808872. [CrossRef]
48. Paul, R.; Zhai, Q.; Roy, A.K.; Dai, L. Charge Transfer of Carbon Nanomaterials for Efficient Metal-Free Electrocatalysis. *Interdiscip. Mater.* **2022**, *1*, 28–50. [CrossRef]
49. Peng, H.-J.; Hou, T.-Z.; Zhang, Q.; Huang, J.-Q.; Cheng, X.-B.; Guo, M.-Q.; Yuan, Z.; He, L.-Y.; Wei, F. Strongly Coupled Interfaces between a Heterogeneous Carbon Host and a Sulfur-Containing Guest for Highly Stable Lithium-Sulfur Batteries: Mechanistic Insight into Capacity Degradation. *Adv. Mater. Interfaces* **2014**, *1*, 1400227. [CrossRef]
50. Wang, Y.; Adekoya, D.; Sun, J.; Tang, T.; Qiu, H.; Xu, L.; Zhang, S.; Hou, Y. Manipulation of Edge-Site Fe-N_2 Moiety on Holey Fe, N Codoped Graphene to Promote the Cycle Stability and Rate Capacity of Li-S Batteries. *Adv. Funct. Mater.* **2019**, *29*, 1807485. [CrossRef]
51. Li, Y.; Chen, G.; Mou, J.; Liu, Y.; Xue, S.; Tan, T.; Zhong, W.; Deng, Q.; Li, T.; Hu, J.; et al. Cobalt Single Atoms Supported on N-Doped Carbon as an Active and Resilient Sulfur Host for Lithium-Sulfur Batteries. *Energy Storage Mater.* **2020**, *28*, 196–204. [CrossRef]
52. Kim, H.; Lee, J.; Ahn, H.; Kim, O.; Park, M.J. Synthesis of Three-Dimensionally Interconnected Sulfur-Rich Polymers for Cathode Materials of High-Rate Lithium–Sulfur Batteries. *Nat. Commun.* **2015**, *6*, 7278. [CrossRef] [PubMed]
53. Cheng, Z.; Pan, H.; Chen, J.; Meng, X.; Wang, R. Separator Modified by Cobalt-Embedded Carbon Nanosheets Enabling Chemisorption and Catalytic Effects of Polysulfides for High-Energy-Density Lithium-Sulfur Batteries. *Adv. Energy Mater.* **2019**, *9*, 1901609. [CrossRef]
54. Huang, X.; Tang, J.; Luo, B.; Knibbe, R.; Lin, T.; Hu, H.; Rana, M.; Hu, Y.; Zhu, X.; Gu, Q.; et al. Sandwich-Like Ultrathin TiS_2 Nanosheets Confined within N, S Codoped Porous Carbon as an Effective Polysulfide Promoter in Lithium-Sulfur Batteries. *Adv. Energy Mater.* **2019**, *9*, 1901872. [CrossRef]
55. Li, Y.; Zhou, P.; Li, H.; Gao, T.; Zhou, L.; Zhang, Y.; Xiao, N.; Xia, Z.; Wang, L.; Zhang, Q.; et al. A Freestanding Flexible Single-Atom Cobalt-Based Multifunctional Interlayer toward Reversible and Durable Lithium-Sulfur Batteries. *Small Methods* **2020**, *4*, 1900701. [CrossRef]
56. Mu, J.; Zhang, M.; Li, Y.; Dong, Z.; Pan, Y.; Chen, B.; He, Z.; Fang, H.; Kong, S.; Gu, X.; et al. Laser Irradiation Constructing All-in-One Defective Graphene-Polyimide Separator for Effective Restraint of Lithium Dendrites and Shuttle Effect. *Nano Res.* **2023**, *16*, 12304–12314. [CrossRef]